

## Determination of the Noninductive Current Profile in Tokamak Plasmas

C. B. Forest, K. Kupfer,\* T. C. Luce, P. A. Politzer, L. L. Lao, M. R. Wade,† D. G. Whyte,‡ and D. Wróblewski§

General Atomics, San Diego, California 92186-9784

(Received 19 May 1994)

The noninductive part of the measured current profile has been determined for DIII-D plasmas. A technique for determining the flux surface average of the quantity  $\mathbf{E} \cdot \mathbf{B}$  and a model for the resistivity separates the current profile into inductive and noninductive portions. Analysis shows directly that neoclassical resistivity is adequate to explain the experimental observations, while Spitzer resistivity is not, and that a large noninductive current exists in plasmas for which large neutral beam current drive and pressure driven bootstrap currents are expected.

PACS numbers: 52.55.Fa

Currents driven noninductively improve the feasibility of the tokamak fusion reactor concept in several ways. These currents not only offer the possibility of operating a tokamak in steady state, but may also lead to improvements in tokamak performance, i.e., confinement properties and stability limits, through control of the current profile [1–3]. The tokamak current can be maintained noninductively by unidirectional rf waves or neutral beam injection. At present, results from noninductive current drive experiments using these methods of auxiliary current drive imply that a large fraction of the output power from a reactor will be necessary to maintain the plasma current in conventional reactor scenarios. However, auxiliary power requirements may be reduced to acceptable levels by operating in regimes with a large fraction of bootstrap current [4], noninductive current driven by pressure gradients. In this scenario, auxiliary driven current in addition to the pressure driven bootstrap current is expected to be necessary to obtain a stable current profile. To effectively combine the auxiliary driven noninductive currents and the bootstrap current for improved tokamak operation, information about the magnitude and profile of each noninductive current source (e.g., bootstrap current profile or neutral beam driven current profile) is needed.

In this Letter a technique for determining the noninductive current profile in a tokamak plasma is presented and applied to two example DIII-D tokamak discharges. Central to this technique is the determination of the current density profile  $j(\rho)$  from measurements and equilibrium reconstructions [5] and a method for determining the parallel electric-field profile ( $\rho$  is a coordinate representing minor radius). By determining the internal electric-field profile and calculating the resistivity profile on the basis of measurements of the temperature profile  $T_e(\rho)$  and effective charge  $Z_{\text{eff}}(\rho)$ , the inductive current density  $j_{\text{oh}}(\rho)$  can be calculated and compared with the measured current density: The noninductive portion of the current is the difference between  $j(\rho)$  and  $j_{\text{oh}}(\rho)$ . Furthermore, if the noninductively driven current is small or if the noninductive current profile is assumed to be known, this measurement provides a local test of the resistivity model.

The magnetic field  $\mathbf{B}$  inside an axisymmetric tokamak plasma can be described by

$$\mathbf{B} = F(\psi)\nabla\phi + \nabla\psi \times \nabla\phi, \quad (1)$$

where the cylindrical coordinate system  $(R, Z, \phi)$  is used,  $\psi = -\int_0^R B_Z R' dR'$  is the total poloidal flux per radian inside a major radius  $R$ , and  $F(\psi) = RB_\phi$ . Furthermore, it is assumed that toroidally symmetric, nested flux surfaces exist and can be labeled by either  $\psi$  or the enclosed toroidal flux  $\Phi = \int_V d^3x \mathbf{B} \cdot \nabla\phi$ , related by the equation  $2\pi q(\psi) \equiv d\Phi/d\psi$ . The local toroidal inductive electric field ( $E_\phi$ ) is related to the poloidal flux by  $RE_\phi(R, Z) = \partial\psi/\partial t|_{R, Z}$ . With measurements of the poloidal flux on the vessel wall, and measurements of the vertical field vs time inside the vessel, the changing flux can be integrated to determine the  $E_\phi$  at a fixed spatial position. This shows the basis for a measurement of the  $E$  but does not provide the value of  $E_{\parallel}$  (only  $E_\phi$ ) and only gives a measurement at a fixed point.

In a general toroidal geometry, the equation relating the current density to the electric field is

$$\langle \mathbf{j} \cdot \mathbf{B} \rangle = \eta^{-1} \langle \mathbf{E} \cdot \mathbf{B} \rangle + \langle \mathbf{j}_{\text{NI}} \cdot \mathbf{B} \rangle, \quad (2)$$

where  $\langle A \rangle$  is the flux surface average of  $A$ ,  $\eta$  is the parallel resistivity, and  $\mathbf{j}_{\text{NI}}$  represents any sources of noninductive current drive (including both bootstrap current and auxiliary driven currents). The flux surface average of the quantity  $\langle \mathbf{E} \cdot \mathbf{B} \rangle$  can be shown to be [6]

$$\langle \mathbf{E} \cdot \mathbf{B} \rangle = \frac{\langle B_\phi^2 \rangle}{F} \frac{\partial\psi}{\partial t} \Big|_{\Phi}. \quad (3)$$

In this equation, the derivatives of poloidal flux are taken on surfaces of constant toroidal flux  $\Phi$ . Thus the electric field is related solely to changes in poloidal flux, while the flux surface label  $\Phi$  provides a proper reference frame in which no poloidal electric fields are induced from changes in toroidal flux. It is convenient to define an effective parallel electric field  $\mathcal{E}_{\parallel} = \langle \mathbf{E} \cdot \mathbf{B} \rangle / B_{r0}$ , which replaces  $\langle \mathbf{E} \cdot \mathbf{B} \rangle$  in the following calculations.  $2\pi R_0 \mathcal{E}_{\parallel}$  reduces to the toroidal loop voltage in the limit of large aspect ratio, where  $B_{r0}$  is the vacuum field at the center of the vessel ( $R_0$ ). In addition, the flux surface label  $\rho$

defined as  $(\Phi/B_{T0}\pi)^{1/2}$  is used rather than  $\Phi$ ; note,  $\rho$  has units of length.

To calculate  $\mathcal{E}_{\parallel}$  for noncircular plasmas, the current density profiles and  $\psi(R, Z)$  are first determined by fitting a solution of the Grad-Shafranov equation to measured quantities at several instances in time. Here, the code EFITD [7] is used. The reconstructions are constrained by measured values of the poloidal field and flux on the vacuum vessel wall, external coil currents, internal pitch angle measurements near the midplane of the tokamak, and measurements of electron and ion densities and temperature for the scalar pressure  $p(\psi)$ . As a result of the reconstructions, the quantities  $q(\psi)$ ,  $F(\psi)$ ,  $B_{\phi}(R, Z)$ , and  $\psi(R, Z)$  are determined at each time and  $\psi(\rho)$  can be easily calculated. Once  $\psi(\rho, t)$  is known for a time sequence of equilibria, then  $\mathcal{E}_{\parallel}$  can be calculated from Eq. (3).

Once  $\mathcal{E}_{\parallel}$  has been determined from several equilibria, an error analysis is necessary to estimate the uncertainties in  $\mathcal{E}_{\parallel}$ . Uncertainties in  $\mathcal{E}_{\parallel}$  [or  $\psi(\rho, t)$ ] and  $\langle \mathbf{j} \cdot \mathbf{B} \rangle$  arise from several possible sources of error. To estimate the effect of statistical uncertainties, a Monte Carlo approach is used in which the equilibrium is recalculated with each input datum to EFITD randomly perturbed with a distribution characterized by the measurement's standard deviation. Calculating a large number (typically 50) of such equilibria then allows the standard deviation of the desired parameters to be calculated, e.g.,  $\sigma_{\psi}(\rho)$ ,  $\sigma_F(\rho)$ , etc. (typical uncertainties are shown on the figures which follow). Such calculations show that the central current density is typically known with a 10% uncertainty, while the poloidal flux is known more accurately, with a 2% to 3% uncertainty. Changes in the parametrization used model for the current density profile [7] (the dominant systematic error) can change the local structure of the current profile (up to 10%), but they have little effect on local values of  $\psi$  (which changes by less than 3%). In general, the error analysis has shown that  $\psi$  can be determined more accurately than  $j$ , which is consistent with  $\psi$  being related to  $j$  by a double integration.

Although  $\psi$  is well constrained for a particular equilibrium, the derivative of  $\psi$  with respect to time can be a very small number if the plasma is hot, in which case even small uncertainties in  $\mathcal{E}_{\parallel}$  may be significant when determining  $j_{\text{oh}}$ . Assuming statistical errors, the uncertainty in  $\mathcal{E}_{\parallel}$  can be written approximately as

$$\sigma_{\mathcal{E}_{\parallel}} = \sqrt{\sigma_G^2 \left( \frac{\partial \psi}{\partial t} \right)^2 + 2G^2 \left( \frac{\sigma_{\psi}}{\Delta t} \right)^2}, \quad (4)$$

where  $G = \langle B_{\phi}^2 \rangle / FB_{T0}$  is a geometric term and  $\Delta t$  is the time step between equilibrium reconstructions. Increasing  $\Delta t$  reduces the uncertainty in  $\mathcal{E}_{\parallel}$ , but also decreases the time resolution of the measurement. The factor of 2 comes from propagating the errors through the finite difference of  $\psi$  in Eq. (3) to determine  $\partial \psi / \partial t$ ; it is this term which dominates the error in  $\mathcal{E}_{\parallel}$  for the cases studied thus far. The uncertainty in calculating the inductive current (assuming  $\eta \propto Z_{\text{eff}}/T_e^{3/2}$ ) is affected by errors in

the measurements of  $T_e$  and  $Z_{\text{eff}}$  and can be calculated by adding the errors in these measurements and the uncertainty of  $\mathcal{E}_{\parallel}$  in quadrature. The error in determining the noninductive current, the difference between  $j(\rho)$  and  $j_{\text{oh}}(\rho)$ , is then  $(\sigma_{j_{\text{oh}B}}^2 + \sigma_{j_{\parallel B}}^2)^{1/2}$ .

Two DIII-D discharges are examined in this paper to illustrate the technique. In the first discharge the plasma current is dominated by inductive current drive so that this shot can be considered a test of the resistivity model. This discharge is a hot ion  $L$  mode [8] with a positive current ramp, examined during the phase following the current ramp. The second plasma is a low current, high poloidal beta ( $\beta_p$ ) plasma, expected to have a large fraction of noninductive current in the form of bootstrap current and neutral beam driven current [9]. Both plasmas are heated by neutral beam injection, which also provides a means of measuring the local pitch angle of the magnetic field inside the plasma by motional Stark effect (MSE) spectroscopy [10]. In addition, both plasmas have  $q_0 > 1$  and current profiles which are gradually changing in time. The high  $\beta_p$  and  $I_p$  ramp discharges, as well as time sequences analyzed, have been chosen to be free of magnetohydrodynamic (MHD) activity (as determined from fluctuations detected by probes on the vessel wall) and sawtooth relaxations, since these fluctuations could complicate the electric field determination [11].

The hot ion,  $L$ -mode discharge was limited on the inner wall, had a major radius of 1.63 m, a minor radius of 0.62 m, and an elongation of 1.7. Neutral beam heating with a power of 4.6 MW was applied, starting at 1.5 and 3.1 sec; the plasma current was increased from 500 kA to 1.2 MA in a current ramp of 0.2 sec duration. Before the current ramp, the central electron temperature  $T_e$  was 3.2 keV, ion temperature  $T_i$  was 4.2 keV, and electron density  $n_e$  was  $3.5 \times 10^{13} \text{ cm}^{-3}$ ; after the current ramp  $T_e = 3.5 \text{ keV}$ ,  $T_i = 5.5 \text{ keV}$ , and  $n_e = 3.0 \times 10^{13} \text{ cm}^{-3}$ .  $\beta_p$  changed from 1.4 before the current ramp to 0.3 following the current ramp, and thus little bootstrap current was expected during this slowly evolving phase following the current ramp. Calculations of beam driven current and bootstrap current have been made, from which it is estimated that the noninductive current fraction is less than 20% and that the local noninductive current density is less than 30% of the total current density throughout the plasma.

The time evolution of the current profile and associated poloidal flux profile is illustrated in Fig. 1. Figure 1(a) shows that the current was initially peaked compared to later times, and that immediately following the current ramp (3.35 sec), the current profile has broadened, with a large fraction of the current being driven into the periphery of the plasma. Subsequently, this broad profile relaxes to the final profile at 4.06 sec. Throughout this phase  $q_0 \geq 1$  and no sawteeth were observed. In Fig. 1(b), relative changes in the poloidal flux are seen to be much larger than the associated uncertainties (which are within the width of the line  $\psi$ ), so that  $\partial \psi / \partial t$  can be calculated accurately. The difference between the first two profiles is

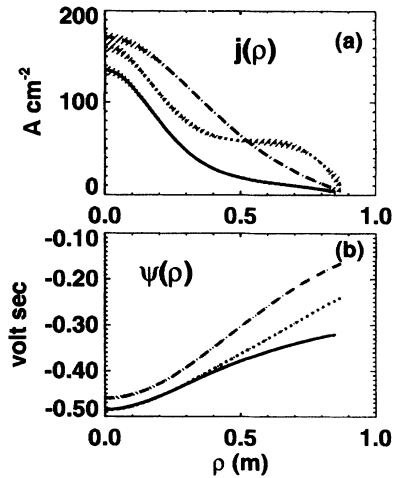


FIG. 1. Equilibrium reconstructions of the (a) current profile  $j(\rho)$  and (b) poloidal flux  $\psi(\rho)$ , for current ramp shot. Solid = 3.05 sec (immediately before ramp), dot = 3.35 sec (immediately following current ramp), and dash = 4.06 sec (after resistive relaxation).

nearly zero at the center, while on the boundary it was quite large, consistent with the measured loop voltage of 3.5 V (determined from a flux loop on the vessel wall) during the current ramp.

The inductive current profile has been determined from three equilibria calculated during the period spanning 3.5 to 4.0 sec. The profile of the loop voltage ( $V = 2\pi R_0 \mathcal{E}_{\parallel}$ ), shown in Fig. 2(a), has not yet equilibrated, with the central value being lower than the value on the periphery. The total current profile and the inductive current determined from Spitzer resistivity and from neoclassical resistivity [12] are shown in Fig. 2(b). The profiles of  $T_e$  were determined by Thomson scattering

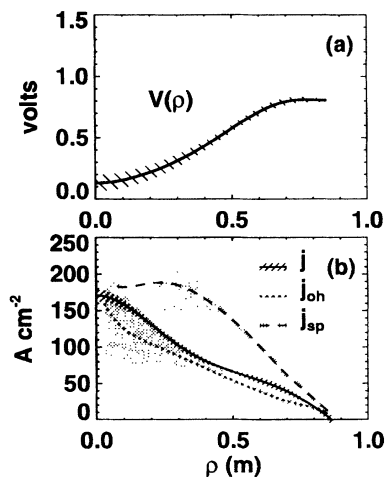


FIG. 2. (a) The loop voltage profile determined for the interval  $t = 3.5$  to 4.0 sec, and (b) the measured current profile (averaged over the same period) compared to the inductive current profile predicted from neoclassical resistivity ( $j_{oh}$ ) and Spitzer resistivity ( $j_{sp}$ ) for the discharge in Fig. 1. The difference between the total current and Ohmic current is the noninductive current, a combination of bootstrap current and neutral beam current drive.

2446

and electron cyclotron emission (ECE). To determine the profile of  $Z_{eff}$ , the carbon density profile (shown to be the predominant impurity by survey spectrometers) has been determined by charge-exchange recombination spectroscopy. The profiles of  $Z_{eff}$  have been confirmed by visible bremsstrahlung measurements. Typically,  $T_e$  is measured with 5% accuracy, while  $Z_{eff}$  is deduced within  $\pm 10\%$ , predominantly due to uncertainties in the density profile. The profiles of total current and neoclassical inductive current are similar in magnitude and shape. The difference between the two curves—the noninductive current—is easily accounted for by calculations of the small noninductive current density from bootstrap current and neutral beam current drive. In contrast, Spitzer resistivity overestimates the current density by approximately a factor of 2 for much of the plasma. From this we conclude that the neoclassical resistivity model is sufficiently accurate for analyzing other discharges, in which the noninductive current may be a larger fraction of the total current.

The high- $\beta_p$  ( $\beta_p > 3$ ) DIII-D discharge was an elongated ( $\kappa = 2.1$ ), high triangularity ( $\delta = 0.9$ ) shape, with a plasma current of 400 kA and 8 MW of neutral beam heating starting at 1 sec. The central electron temperature was approximately 2.5 keV, the central density was  $3.5 \times 10^{13} \text{ cm}^{-3}$ , and  $Z_{eff} \sim 2$ . Following the start of beam injection, the current profile resistively relaxed as  $q_0$  increased from  $\sim 1$  at 1 sec to  $> 2$  at 3 s.

Profiles of  $\psi$ ,  $j$ , and  $2\pi R_0 \mathcal{E}_{\parallel}$  for three instances in time (1.4, 2.15, and 2.75 sec) are shown in Fig. 3. The shaded region represents the uncertainty from the reconstruction, which shows the profiles are better determined near the periphery than the central region. Figure 3(b) shows details of the changing current profile. Corresponding to the changing current profile, the shape of  $\psi(\rho)$  is also changing with time, as shown in Fig. 3(a). For this discharge, as in the previous discharge, the changes are much larger than the uncertainty in determining  $\psi(\rho)$ , allowing for an accurate calculation of the loop voltage, as shown in Fig. 3(c). Distinguishable changes occur in the calculated loop voltage profile as it flattens from the initially peaked value. Figure 3(c) also shows the values of the loop voltage as measured by a flux loop on the vessel wall (represented by diamonds) indicating that the calculated loop voltage profile is consistent with this measurement. Early in time it is clear that the calculated electric field on axis is positive while the at the edge it is negative, maintaining the initially peaked current profile. Late in the shot as the plasma approaches resistive equilibrium, a uniform electric field is calculated.

The experimentally measured current density  $j(\rho)$  and the noninductive current density profile  $j_{NI}(\rho)$  determined from the difference between  $j(\rho)$  and  $j_{oh}(\rho)$ , the calculated current density based on neoclassical resistivity, are shown in Fig. 4. The current density is dominated by noninductive effects outside  $\rho > 0.1$ . Also shown in Fig. 4 are the calculated bootstrap current and the sum

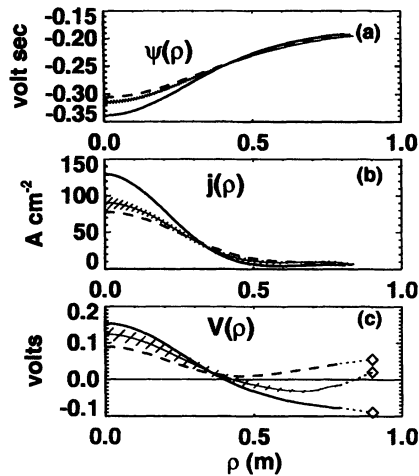


FIG. 3. Equilibrium reconstructions of the poloidal flux  $\psi(\rho)$ ,  $j(\rho)$ , and the internal loop voltage profile  $2\pi R_0 \mathcal{E}_{\parallel}(\rho)$ . Solid = 1.4 sec, solid + shading = 2.15 sec, and dashed = 2.75 sec. The shading for  $t = 2.15$  sec is representative of the uncertainty for the other times. The diamonds are the measured loop voltage on the vessel wall. The discharge is the high  $\beta_p$  discharge described in the text.

of bootstrap and the calculated neutral beam driven current [13,14]. The estimation of the total noninductive current from the calculations is in general agreement with the exception of the central region, which shows less beam driven current than the model predicts.

In summary, a method for determining the noninductive current profile in tokamak plasmas has been developed. The quantity  $\langle \mathbf{E} \cdot \mathbf{B} \rangle$  can be determined with sufficient accuracy and combined with the calculated neoclassical resistivity to determine the inductive portion of the current profile. The total reconstructed current profile can thus be separated into inductive and noninductive portions. To

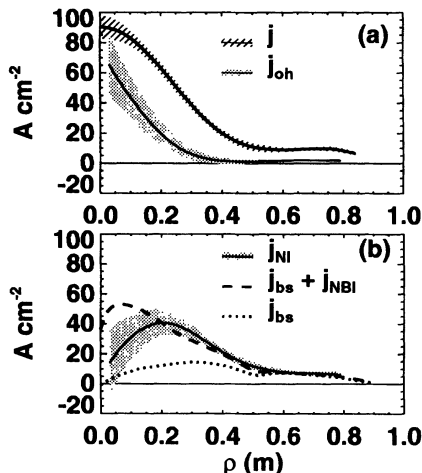


FIG. 4. (a) The measured and calculated inductive current density, (b) noninductive current density  $j_{NI}$  determined from the difference from (a), and the calculated noninductive current due to neutral beam injection and bootstrap current ( $j_{BS} + j_{NBI}$ ), for the discharge in Fig. 3 during the period 2.15 to 2.95 sec.

investigate the relationship between current and electric field, two neutral beam heated discharges from different parameter regimes have been investigated to establish the validity of a neoclassical resistivity model and, then, to use this verified model to calculate the profiles of noninductive current in plasmas with a high value of  $\beta_p$ . By the technique used here, it is not possible to distinguish between the various sources of noninductive current—it is only possible to determine the net noninductive current. We find that for the example discharge, the model based calculations of these currents are similar to the experimentally determined noninductive currents, but that the neutral beam driven current is somewhat overestimated in the center of the plasma. These and future experiments will further characterize noninductive current profiles, possibly allowing for current profile control and advance tokamak operating regimes.

This is a report of work sponsored by the U.S. Department of Energy under Contract No. DE-AC03-89ER51114, DE-AC05-84OR21400, and W-7405-ENG-48, and by an appointment to the Fusion Energy Postdoctoral Research Program at General Atomics, administered by the Oak Ridge Institute for Science and Education.

\*Permanent address: Oak Ridge Institute for Science and Education Fellow at General Atomics.

†Permanent address: Oak Ridge National Laboratory, Oak Ridge, Tennessee.

‡Permanent address: Centre Canadien de Fusion Magnétique, Varennes, Québec, Canada.

§Permanent address: Lawrence Livermore National Laboratory, Livermore, California.

- [1] J. R. Ferron *et al.*, Phys. Fluids **5**, 2532 (1993).
- [2] C. Kessel *et al.*, Phys. Rev. Lett. **72**, 1212 (1994).
- [3] A. D. Turnbull *et al.*, "High Beta and Enhanced Confinement in a Second Stable Core VH-Mode Advanced Tokamak" (to be published).
- [4] M. C. Zarnstorff *et al.*, Phys. Rev. Lett. **60**, 1306 (1988).
- [5] D. Wróblewski and L. L. Lao, Rev. Sci. Instrum. **63**, 5140 (1992).
- [6] F. L. Hinton and R. D. Hazeltine, Rev. Mod. Phys. **48**, 239 (1976).
- [7] L. L. Lao *et al.*, Nucl. Fusion **20**, 1025 (1990).
- [8] K. H. Burrell *et al.*, in *Plasma Physics and Controlled Nuclear Fusion Research 1990*, Proceedings of the 13th International Conference, Washington, 1990 (IAEA, Vienna, 1993), Vol. 1, p. 123.
- [9] P. A. Politzer *et al.*, Phys. Plasmas **1**, 1944 (1994).
- [10] D. Wróblewski and L. L. Lao, Rev. Sci. Instrum. **63**, 5140 (1992).
- [11] F. Alladio and G. Vlad, Phys. Fluids **31**, 602 (1988).
- [12] S. P. Hirshman and D. J. Sigmar, Nucl. Fusion **21**, 1079 (1981).
- [13] S. P. Hirshman, Phys. Fluids **31**, 3150 (1988).
- [14] J. D. Callen *et al.*, in *Plasma Physics and Controlled Nuclear Fusion Research 1974*, Proceedings of the 5th International Conference Kyoto, 1974 (IAEA, Vienna, 1975), Vol. 1, p. 645.

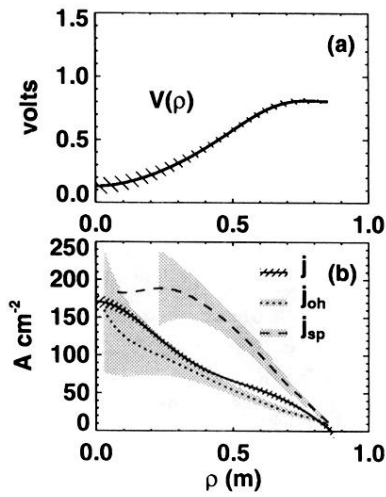


FIG. 2. (a) The loop voltage profile determined for the interval  $t = 3.5$  to  $4.0$  sec, and (b) the measured current profile (averaged over the same period) compared to the inductive current profile predicted from neoclassical resistivity ( $j_{oh}$ ) and Spitzer resistivity ( $j_{sp}$ ) for the discharge in Fig. 1. The difference between the total current and Ohmic current is the noninductive current, a combination of bootstrap current and neutral beam current drive.

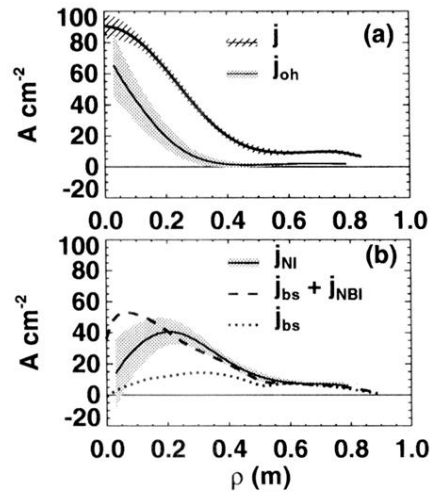


FIG. 4. (a) The measured and calculated inductive current density, (b) noninductive current density  $j_{NI}$  determined from the difference from (a), and the calculated noninductive current due to neutral beam injection and bootstrap current ( $j_{BS} + j_{NBI}$ ), for the discharge in Fig. 3 during the period 2.15 to 2.95 sec.